SAND2021-11464

**SANDIA REPORT**
SAND20XX-XXXX
Printed Click to enter a date

Sandia National Laboratories

# Isotopic fractionation as in-situ sensor of subsurface reactive flow and precursor for rock failure

Anastasia G. Ilgen, R. Charles Choens, Andrew W. Knight, Jacob A. Harvey, Mario J. Martinez, Hongkyu Yoon, Jennifer Wilson, Melissa M. Mills, Qiaoyi Wang, Michael Gruenwald, Pania Newell, Louis Schuler, and Haley J. Davis

Prepared by
Sandia National Laboratories
Albuquerque, New Mexico
87185 and Livermore,
California 94550

Issued by Sandia National Laboratories, operated for the United States Department of Energy by National Technology & Engineering Solutions of Sandia, LLC.



Available to DOE and DOE contractors from

U.S. Department of Energy
Office of Scientific and Technical Information
P.O. Box 62
Oak Ridge, TN 37831

Telephone: (865) 576-8401
Facsimile: (865) 576-5728
E-Mail: reports@osti.gov
Online ordering: http://www.osti.gov/scitech

Available to the public from

U.S. Department of Commerce
National Technical Information Service
5301 Shawnee Rd
Alexandria, VA 22312

Telephone: (800) 553-6847
Facsimile: (703) 605-6900
E-Mail: orders@ntis.gov
Online order: https://classic.ntis.gov/help/order-methods/


DEPARTMENT OF ENERGY
UNITED STATES OF AMERICA
NNSA
National Nuclear Security Administration

## ABSTRACT

Greater utilization of subsurface reservoirs perturbs in-situ chemical-mechanical conditions with wide ranging consequences from decreased performance to project failure. Understanding the chemical precursors to rock deformation is critical to reducing the risks of these activities. To address this need, we investigated the coupled flow-dissolution-precipitation-adsorption reactions involving calcite and environmentally-relevant solid phases. Experimentally, we quantified (1) stable isotope fractionation processes for strontium during calcite nucleation and growth, and during reactive fluid flow; (2) consolidation behavior of calcite assemblages in the common brines. Numerically, we quantified water weakening of calcite using molecular dynamics simulations; and quantified the impact of calcite dissolution rate on macroscopic fracturing using finite element models. With microfluidic experiments and modeling, we show the effect of local flow fields on the dissolution kinetics of calcite. Taken together across a wide range of scales and methods, our studies allow us to separate the effects of reaction, flow, and transport, on calcite fracturing and the evolution of strontium isotopic signatures in the reactive fluids.

## ACKNOWLEDGEMENTS

We acknowledge Makeila Maguire for analyzing scanning electron microscopy images, Mohammad Shohel for X-ray diffraction analysis, Ping Lu for transmission electron microscopy, and Damion Cummings for focused ion beam sample preparation. This work was supported by the Sandia National Laboratories Laboratory Directed Research and Development program, Project No. 212950.

## CONTENTS



## LIST OF FIGURES

## LIST OF TABLES

This page left blank

# ACRONYMS AND DEFINITIONS

| Abbreviation | Definition |
|---|---|
| AE | Acoustic emission |
| BSE | Backscatter electron [images] |
| DFT | Density functional theory |
| ICP-MS | Inductively coupled plasma mass spectrometer |
| MD | Molecular Dynamic [simulations] |
| SEM | Scanning electron microscopy |
| SRM | Standard Reference Material |
| TEM | Transmission electron microscopy |
| XRD | X-ray diffraction |

# 1. INTRODUCTION

The use of subsurface reservoirs for resource extraction, carbon sequestration, nuclear waste disposal, and energy production perturbs the steady-state or equilibrium conditions of these underground systems. The resulting chemical dis-equilibrium drives mineral alteration reactions at the pore-scale, with response from carbonate minerals being geologically rapid (days to months). The *pore-scale* here refers to the scale of individual grains and voids, ranging from nanometers to microns and millimeters in sedimentary rocks. At these scales, all mineral phases and interfaces can be identified, and chemical reactions and hydrodynamic conditions can be discerned; however, transferring the pore-scale knowledge to continuum-scale processes is a major challenge.

Pore-scale mineral dissolution and precipitation reactions are known to lead to macroscopic rock deformation and failure in carbonate-rich sedimentary basins. We postulate that by discerning signals from chemical processes involving carbonate minerals, such as calcite ($CaCO_3$), we could anticipate and predict rock damage and failure at continuum scales. To achieve this goal, we investigated changes in stable isotopic signatures from elements in $CaCO_3$ minerals. Strontium ions ($Sr^{2+}$) commonly substitute for $Ca^{2+}$ in $CaCO_3$, and carbon (C) in the structure of $CaCO_3$; therefore, carbonate dissolution-precipitation could impact Sr, Ca, and C isotopic ratios in the fluid [1]. Fractionation of these stable isotopes has been observed for Ca and Sr during $CaCO_3$ precipitation [2-6], and during $CaCO_3$ replacement by dolomite ($MgCaCO_3$) [7]. In addition to dissolution-precipitation reactions involving carbonates, chemical transport through porous media could also shift the isotopic signatures of the dissolved constituents due to either kinetic or thermodynamic isotope fractionation processes [1]. Isotopic signatures of subsurface fluids are a sum of subsurface mineral transformations, adsorption reactions, and flow processes. We hypothesize that changes in isotopic signatures due to carbonate dissolution-precipitation and reactive transport processes can be interpreted as a precursor to rock failure and deformation. This fundamental understanding of chemical controls on the evolution of isotopic signatures in aqueous fluids can be applied for in-situ monitoring of carbonate mineral dynamics and for inferring and anticipating mechanical degradation of carbonate-cemented rocks.

The goal of our research is to better understand the processes that lead to isotopic fractionation in sedimentary rocks and to test changes in the $^{87}Sr/^{86}Sr$ ratio of subsurface

fluids as an in-situ sensor for early stage rock deformation and failure. To achieve our goal, we: (i) quantified stable isotope fractionation signatures for Sr during nucleation and growth of $CaCO_3$ in the presence and absence of other divalent cations ($Mg^{2+}$); (ii) quantified adsorption of $^{86}Sr$, $^{87}Sr$, and $^{88}Sr$ onto surfaces of common minerals to determine whether $^{87}Sr/^{86}Sr$ ratio of subsurface fluids could be affected by adsorption processes; (iii) quantified consolidation behavior of $CaCO_3$ grain packs in the presence of common salts [8] and background Sr ions to identify chemical effects on fracturing; (iv) used molecular dynamics simulations to infer fracturing mechanisms in $CaCO_3$ exposed to water; (v) used finite element modeling to quantify the effect of $CaCO_3$ dissolution rate on fracturing of sedimentary rocks [9]; and (vi) quantified the effect of local flow fields on the dissolution kinetics of $CaCO_3$ and developed numerical models predicting dissolution rate as a function of fluid flow rate. We used batch reactors, *ab initio* and classical molecular dynamics simulations, and microfluidic flow experiments to separate effects of reaction, flow, and transport, controlling nucleation/growth/dissolution of $CaCO_3$ and partitioning of $^{87}Sr$ and $^{86}Sr$ isotopes within porous media. Each of these topics was summarized in a manuscript either already submitted to a journal or prepared for submission. Each section of this report presents short summaries of these manuscripts. Additionally, our findings on chemical complexation reactions controlling subcritical cracking in $CaCO_3$ is submitted as a Provisional Patent application.

## 2. PUBLICATION IN PREPARATION: DIVALENT CATION INCORPORATION DURING CALCITE CRYSTALLIZATION

To understand shifts in Sr isotopic signatures during calcite dissolution, we first examined how $CaCO_3$ nucleates, aggregates, and grows in batch systems in the presence of divalent cations $Mg^{2+}$ and $Sr^{2+}$. Since Sr isotopic fractionation is dependent on the Sr distribution factor ($D_{Sr}$) in calcite (through ion replacement with $Ca^{2+}$) and the $D_{Sr}$ is dependent upon the chemical environment of calcite precipitation, we evaluated the impact of the presence of other divalent cations (*i.e.* $Mg^{2+}$, which is a common constituent of subsurface fluids) on this substitution reaction and how those impacts affected Sr isotopic fractionation.

The elemental and isotopic composition of $CaCO_3$ mineral is strongly impacted by the chemical environment where crystal nucleation and growth take place [2-4, 10-24]. Current models are incapable of capturing the relationship between the environment where $CaCO_3$ precipitates and the resulting chemical and physical properties of this mineral. In this study, we quantified coupled effects of aqueous $Sr^{2+}$ and $Mg^{2+}$ cations on $CaCO_3$ precipitation and subsequent crystal growth. We used aqueous chemical analysis, scanning electron microscopy (SEM) and transmission electron microscopy (TEM) of $CaCO_3$ grains in conjunction with density functional theory (DFT) calculations to elucidate the relationship between crystal growth and the resulting $CaCO_3$ chemical composition and physical properties. We found that in the presence of $Mg^{2+}$ and $Sr^{2+}$, $CaCO_3$ crystal growth was inhibited; however, the impacts of these cations are different. $Sr^{2+}$ incorporation into $CaCO_3$ lattice is favored over $Mg^{2+}$. Additionally, the incorporation of $Mg^{2+}$ into $CaCO_3$ lattice lead to a reduction in the $CaCO_3$ unit cell volume, whereas incorporation of $Sr^{2+}$ leads to an expansion. When both $Mg^{2+}$ and $Sr^{2+}$ reside in $CaCO_3$ lattice, the unit cell dimensions depend on the relative positions of the $Sr^{2+}$ and $Mg^{2+}$. We demonstrated that the incorporation of the lighter $^{86}Sr$ isotope is favored over the heavier $^{87}Sr$ isotope during the precipitation and growth of $CaCO_3$ crystals, regardless of the initial solution conditions. These results, summarized in Figure 2-1, demonstrate the impact of the bulk solution chemistry and the intricate balance between the resulting calcite elemental composition, the calcite crystal growth behavior -- including crystal sizes, morphology, and lattice parameters--, and the isotopic shift in $^{87/86}Sr$. Quantitative descriptions linking $CaCO_3$ nucleation and crystal growth rates with aqueous chemistry

(namely, concentration and identity of divalent cations other than $Ca^{2+}$) are crucial for developing predictive geochemical signatures arising during dynamic chemo-mechanical processes involving carbonate minerals.

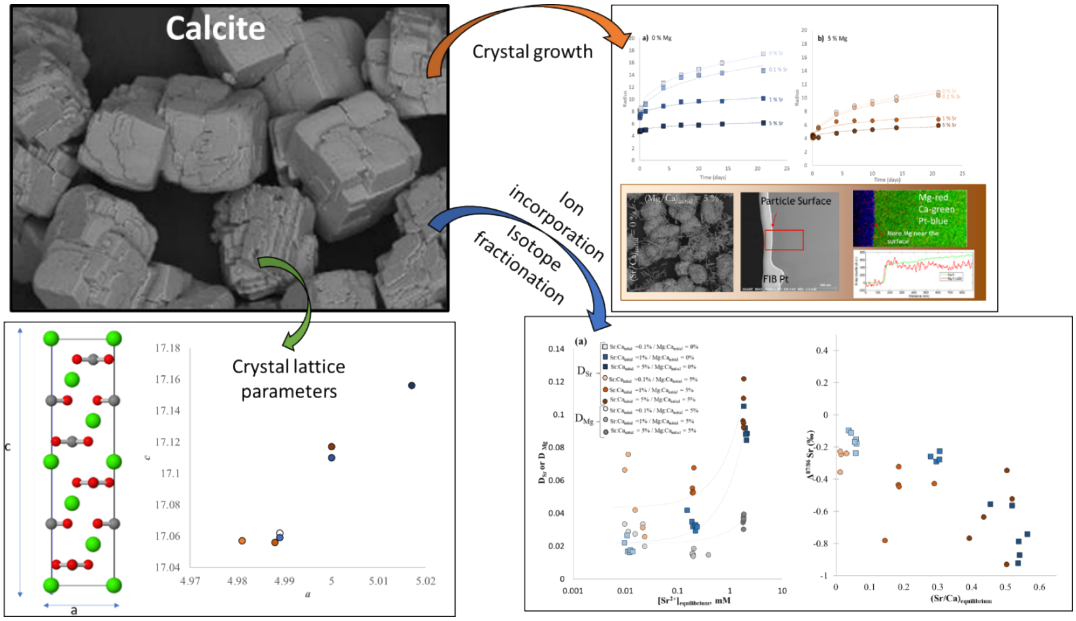


**Figure 2-1. Summary demonstrating the impact of the equilibrium time and initial conditions, with respect to mol fraction of Mg and Sr present, for calcite precipitation and their impact on crystal growth rate and mechanisms; crystal morphologies; crystal lattice parameters and volume; $Sr^{2+}$ and $Mg^{2+}$ ion incorporation behavior; and $^{87/86}$Sr-isotopic fractionation**

## 3. PUBLICATION IN PREPARATION: ADSORPTION OF STABLE STRONTIUM ISOTOPES ON CLAY MINERAL AND ALUMINUM OXIDE SURFACES

Stable Sr isotopic ratios in natural environments are used as geochemical signatures for water flow and mineral alteration reactions. We propose that the $^{88}Sr/^{87}Sr/^{86}Sr$ ratios can also be used to infer damage and failure of carbonate-containing rocks. In order to test whether stable Sr isotopes released into pore waters have identical adsorption behavior (namely, they partition to the same degree onto mineral surfaces), we performed batch adsorption experiments. Our results indicate that $^{86}Sr$, $^{87}Sr$, and $^{88}Sr$ exhibit subtle fractionation during adsorption reactions on the surfaces of clay minerals and aluminum oxides. We attribute this fractionation to thermodynamic isotope effects – where the resulting adsorption product with heavier $^{88}Sr$ isotope is more thermodynamically stable than the adsorption product with a lighter isotope. Even though this fractionation is subtle in the examined batch systems, our continuum reactive transport models indicate that Sr isotope fractionation due to adsorption reactions may be amplified along reactive path lengths characteristic to geologic systems (Figure 3-1).

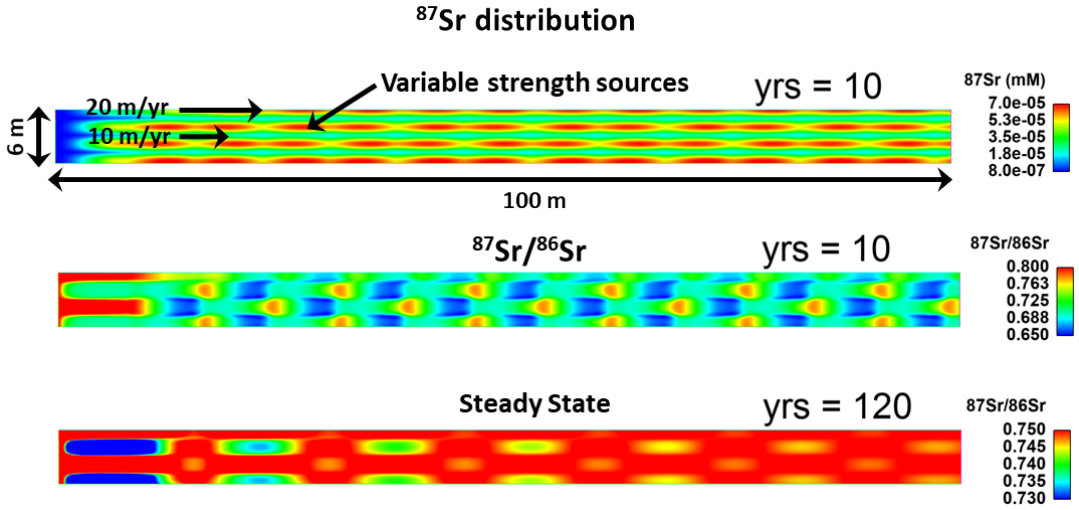


**Figure 3-1. Sr adsorption and mixing from spatially distributed variable sources in porous material containing clay minerals.**

# 4. CHEMICAL COMPLEXATION REACTIONS IN CALCITE CRACK TIPS

## 4.1. Publication in Review: Strengthening of Calcite Assemblages through Chemical Complexation Reactions

This manuscript is currently (as of September 15, 2021) in review at the journal *Geophysical Research Letters*. Calcite is among the most abundant minerals in the Earth's sedimentary rock masses; however, the chemical effects on subcritical fracturing of calcite are poorly understood. Microscopic subcritical cracks in calcite could control reservoir-scale processes such as deformation and subsidence. This study quantifies the effect of chemical complexation reactions at the crack tip of $CaCO_3$ using laboratory experiments on granular calcite assemblages.

In this study we utilized consolidation paths of grain packs under increasing hydrostatic pressure to induce widespread intergranular fracturing in the presence of fluid containing common anions, including chloride, sulphate, and bicarbonate. We also tested consolidation behavior in the presence of citrate anions. These anions were chosen in the order of complexation affinity for $Ca^{2+}$ on the calcite surface. We expected the following strength sequence for our sodium salts based on our hypothesis: $Na_3C_6H_5O_7 > Na_2SO_4 > NaCl > NaHCO_3$. We used petrographic analysis on granular samples before and after consolidation to quantify total fracture densities and characteristics of the damage. Our cumulative results show that molecular-scale chemical complexation reactions at the crack tips of $CaCO_3$ define the growth of subcritical cracks and therefore consolidation at pressures typical for geologic formations. Our findings have broad geoscience implications due to the abundance of carbonates in the subsurface and their economic impact on conventional and unconventional petroleum formations, $CO_2$ enhanced oil recovery projects, and carbon sequestration sites. Our work provides new mechanistic insight, showing that chemical complexation reactions within $CaCO_3$ crack tips define effective fracture toughness, and, by extension, the consolidation behavior of $CaCO_3$ grain packs at pressure conditions typical to subsurface reservoirs.

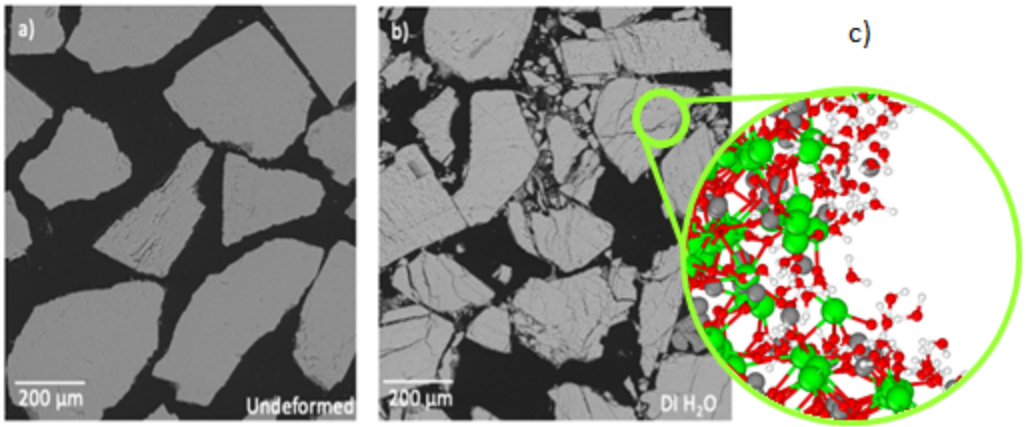


**Figure 4-1. (a) Unconsolidated calcite grains; (b) Fractured calcite grains after consolidation; (c) Molecular representation of calcite crack tip in the presence of water molecules.**

## 4.2. Patent Application: Systems and Methods for Controlling Subcritical Fracturing via Chemical Complexation Reactions at the Crack Tip

The Provisional Patent Application SD15492 was filed in December 2020 [8]. In summary, the filed disclosure describes systems and methods for controlling the propagation of subcritical cracks in crystalline and amorphous solids. The chemical mechanism which affects subcritical cracking described in this disclosure is the same chemical complexation mechanisms at the crack tip as described above in section 4.1.

## 4.3. Preliminary Testing: Strontium Isotopic Ratio in Deforming Calcite-Quartz Assemblages

### *4.3.1. Materials and Methods: Consolidation of Calcite-Quartz Assemblages*

Experiments were performed on assemblages of granular calcite and quartz. Calcite grains were mined from natural formations and sourced from a commercial vendor. The starting material was sieved into a 180 to 300 micron grain distribution. Quartz grains were also sourced from a natural source and sieved to a grain size distribution of 210 to 297 microns. 20.0 gm of calcite and 20.0 gm of quartz were used to make a 40.0 gm sample. To ensure an even distribution of the calcite and quartz grains, each material was alternately poured into a test tube a few grams at a time. The test tube was sealed and rotated about its horizontal axis at a low speed to mix the sample. The resulting mix was poured into a preformed 25 mm diameter polyolefin jacket attached to a titanium endcap. The other endcap was placed into the open end of the jacket with an additional layer of polyolefin. Jackets were attached to the endcaps using nickel-chrome tie wires. Hastelloy frits separated grains from the endcaps and pore lines. Resulting grain packs were 45 mm

in length. Experiments were conducted with 10mM NaCl brine with added Sr isotopes to ~20 ppb concentration. Standard Reference Material (SRM) 987 was used to constrain the initial $^{88}Sr/^{87}Sr/^{86}Sr$ ratios.

Grain pack samples were loaded into a hydrostatic pressure vessel with independent confining and pore fluid systems. The system was initially pressurized to 0.52 MPa before saturating the sample. After pressure stabilized at 0.52 MPa, pore fluid was introduced into the sample at 1 mL/min flow rate through the lower end cap. Fluid flowed out of the top of the sample through an open line to ensure full saturation. After saturation, the open line was connected to a valve attached to a zero-leak back pressure regulator. The valve was closed for the initial pressurization. Confining pressure ($P_C$) was raised to 1.1 MPa, and pore pressure ($P_P$) was raised to 1 MPa in 0.25 MPa steps to ensure that the effective pressure, $P_E = P_C - P_P$, did not exceed the initial 0.52 MPa, preventing further consolidation. The system was held for 14-16 hours to allow pressure and saturation to equilibrate. A piezoelectric transducer was affixed to the exterior of the vessel to monitor for acoustic emissions (AE). Signals were amplified by 60 dB using an inline preamplifier. Post-test, the AE data was reprocessed to a 23 dB threshold with a bandpass filter of 150-750 kHz.

Two experiments were performed in this study, one consolidation experiment and one control experiment. At the start of the consolidation experiment, confining pressure was raised to 1.25 MPa while pore pressure was maintained at 1 MPa. The sample was loaded by raising the confining pressure in 0.5 MPa increments every 5 minutes while pore pressure was constant. Change in fluid volume on the pore pressure pump was used to calculate changes in sample volume. The sample was loaded to a maximum effective pressure of 14.25 MPa. The sample was unloaded in 0.5 MPa increments every 5 minutes. The inline back pressure regulator on the downstream pore fluid line was used to sample pore fluid for geochemical analysis periodically throughout the experiment. The back pressure on the regulator was set to 1.15 MPa to ensure a no flow condition through the regulator during consolidation. To sample pore fluid, the confining pressure was lowered by 1.5 MPa to prevent further deformation during sampling. The control mode on the pore fluid pump was changed from constant pressure to constant flow. Fluid was flowed through the sample at 1.0 mL/min. The first 0.5 mL of sample were discarded, the next 5 mL were sampled, and 5 mL were flushed into a cumulative outflow container for all sample intervals. The initial 0.5 mL ensures that fluid standing in the pore lines was

ignored, and the final 5 mL ensures the pore fluid in the sample was exchanged with fresh fluid. Samples were preserved with 10 µL of 6N ultrapure nitric acid. Another 10 mL of outflow was cleared from the lines before continuing to ramp up confining pressure. ICP-MS is used to quantify $^{86}Sr$ and $^{87}Sr$ in outflow samples. Fluid samples were taken every 3 MPa, which corresponds to 6 pressurization steps, or 30 minutes.

For the control experiments, the initial loading procedure and first sampling interval was the same as the consolidation experiment. At the beginning of the experiment, the confining pressure was increased to 1.25 MPa from the initial value of 1.1 MPa while pore pressure was maintained at 1 MPa, and this effective pressure was held for the experiment. Fluid samples were taken every 30 minutes, which corresponds to the amount of time that it took to ramp up by 3 MPa during the consolidation experiment. The last sample was taken after 145 minutes, again representing the time it took to unload during the consolidation experiment.

Standard petrographic thin sections, 27 x 46 mm and 30 $\mu$m thickness, were prepared for loose grains, control, and consolidated samples. Microscale fracturing and grain interactions were documented in back-scattered electron (BSE) images obtained with a TESCAN Vega3 SEM operated at 30.0 kV. Grain-size distributions, grain perimeters, microporosity, and microfracture densities were quantified with image analysis (through ImageJ) of 1mm x 1mm BSE images. Grain-size distribution was obtained by measuring the diameters of a minimum of 300 grains (entirely contained within each image) per sample. Grain perimeters were captured for these same grains using the Analyze Particles function in ImageJ. Microfracture density ($mm/mm^2$) was quantified by digitally tracing all microfractures observed in 10 BSE images per sample and calculating their cumulative lengths over the image area. Microporosity was calculated from 25 segmented images per sample as the proportion of black (porosity) versus total (porosity + grains) pixels in each image.

### *4.3.2. Results and Discussion: Consolidation of Calcite-Quartz Assemblages*

The consolidation experiment deformed uniformly across the length of the samples and did not show any evidence of localization. The control sample did not show any signs of mesoscopic deformation. Monitored AE during the consolidation experiment shows high levels of activity (~140000 total events at peak loading) (**Figure 4-2**). AE accumulates

slowly at first, then dramatically increases at effective pressures over 6 MPa. Volume strain increases throughout the experiment, indicating consolidation (**Figure 4-3**). Volume strain jumps at sampling intervals, indicating the need for further corrections for switching pore pressure control modes. Initial $^{87}Sr/^{86}Sr$ ratios measured from the overnight pressure equilibration show depressed values compared to the standard. Ratios increase with deformation, reaching a steady value of 0.7 at the from the second sampling interval to the end of the experiment. Dissolution of calcite inferred from the measured Ca concentrations in the sampled fluid are lowest from the overnight pressure hold and increase to maximum value of Ca=62500 ppb at the second sampling interval (**Figure 4-4**). Dissolved Ca concentrations decrease at the end of the experiment.

In the control experiment, AE is negligible as total hits reach 17 at peak load (**Figure 4-2**). Volume strain increases in the control experiment, but volume losses occur during sampling (**Figure 4-3**). Volume strain is steady between sampling intervals; the fluid losses indicate the need for further correction in pore pressure volumes when switching control modes. Strontium isotope ratios after the initial hold are depressed compared to the standard value (**Figure 4-3**). Values briefly drop and then increase for the second sampling interval during the experiment, reaching a steady state value of 0.6. Dissolution of calcite (Ca concentration in the fluid) is also lower for the overnight phase, and then increases during the experiments. Values peak and decline at the third sampling interval of the experiment.

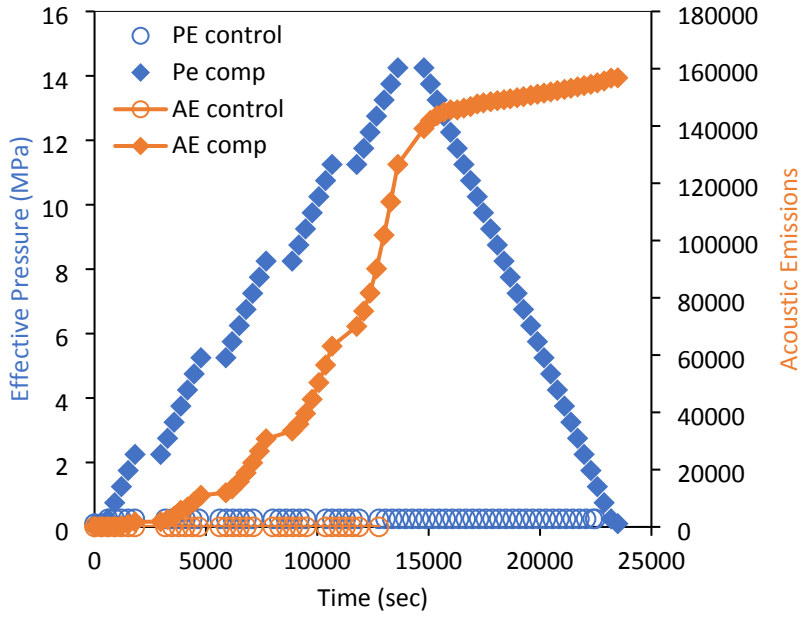


**Figure 4-2. Effective pressure (blue) and acoustic emissions (orange) versus time for consolidation (solid) and control (open) experiments.**

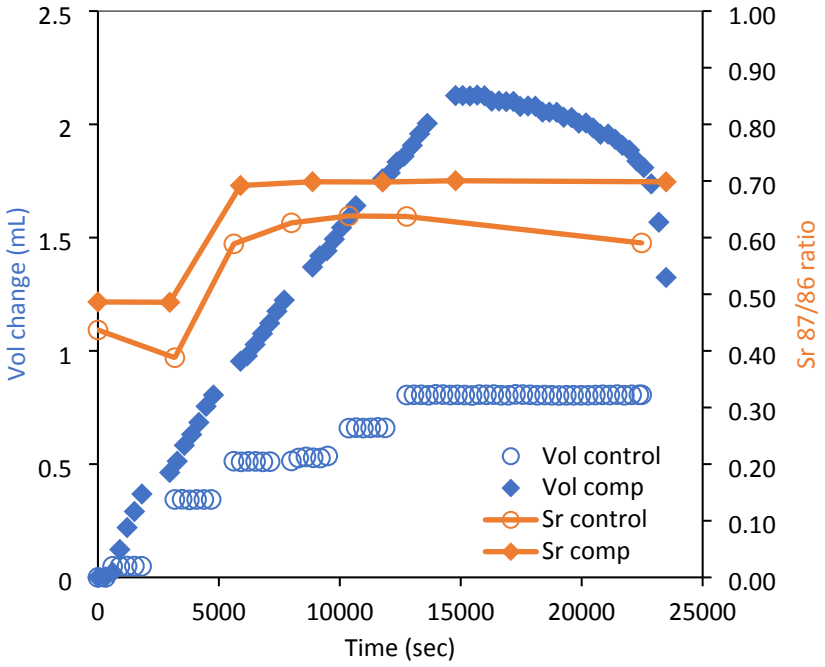


**Figure 4-3. Volume change (blue) and strontium $^{87}Sr/^{86}Sr$ ratio (orange) versus time for consolidation (solid) and control (open) experiments.**

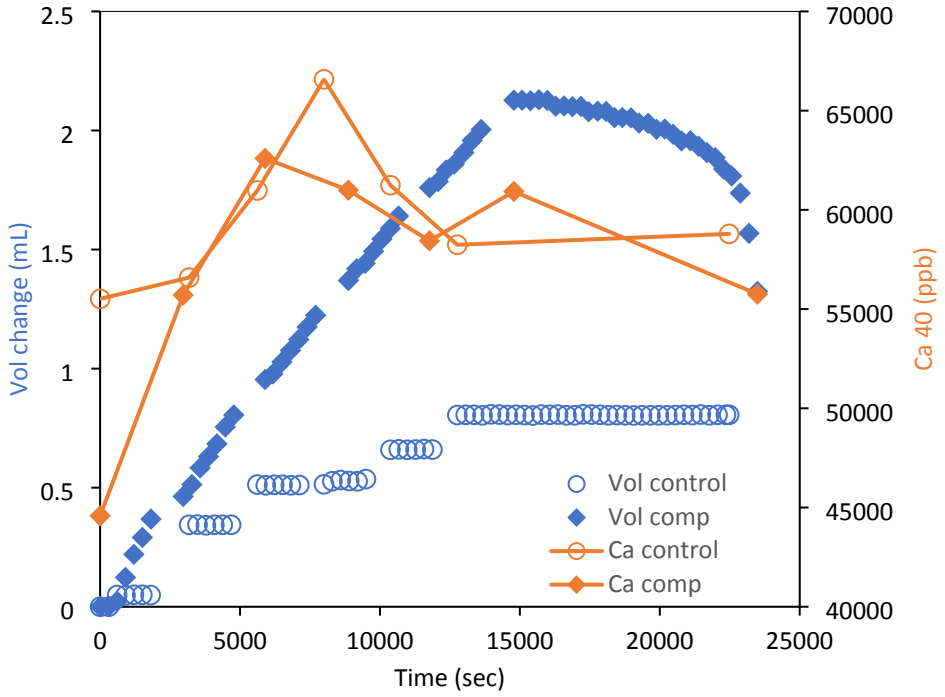


**Figure 4-4. Volume change (blue) and dissolved calcite (orange) versus time for consolidation (solid) and control (open) experiments.**

SEM images of the starting material show quartz grains are usually subrounded to angular while calcite grains are more commonly angular (**Figure 4-5**). With pressurization in control and consolidation experiments, there is an expected increase in grain interaction in these two samples compared to the starting material. Quartz grains (darker gray in SEM images) rarely have pre-existing microfractures in the starting material; microfracture development with flow and consolidation remains minimal in these grains as well (**Figure 4-5**). Microfractures in consolidated quartz grains are commonly due to impingement with adjacent quartz grains and are rarely seen when in contact with calcite grains. Some calcite grains contain pre-existing microfractures, some related to non-activated cleavage, and others that could be attributed to grain settling and handling during sample preparation. In the control experiment, there is an apparent increase in impingement microfracturing of calcite grains, as well as isolated fragmentation and crushing of calcite grains with consolidation (**Figure 4-5**). Impingement microfractures in calcite grains occur when in contact with either quartz or other calcite grains. At some quartz-calcite contacts, impingement is observed to result in more intense damage (grain crushing or fragmentation).

Qualitative observations of reduced pore space, increased microfracturing, and variable grain sizes depending on grain type and experimental conditions are confirmed with image analysis of BSE images from thin sections of each sample (**Figure 4-5**). From the starting material to flow conditions, total microfracture density increases, modal grain diameter for combined grain types decreases, and total grain perimeter increases (**Table 4-1**). Decreases in microporosity and increases in microfracture densities are observed between the flow and consolidation experimental conditions. However, grain-size reduction and grain perimeter are dependent more on grain type (**Figure 4-6**; **Table 4-1**). Grain-size reduction among calcite grains is more pronounced with flow only, and grain-size reduction is greater among quartz grains between the flow experimental conditions and consolidated sample (**Figure 4-6**; **Table 4-1**). The amount of grain perimeter exposed to pore fluid after flow increases for both grain types, but with consolidation, there is an increase for calcite grains and decrease for quartz grains. This may be explained by increases in calcite grain fragmentation leading to partial filling of pore space adjacent to quartz grains (**Figure 4-5**).

Starting Material | Control | Consolidated

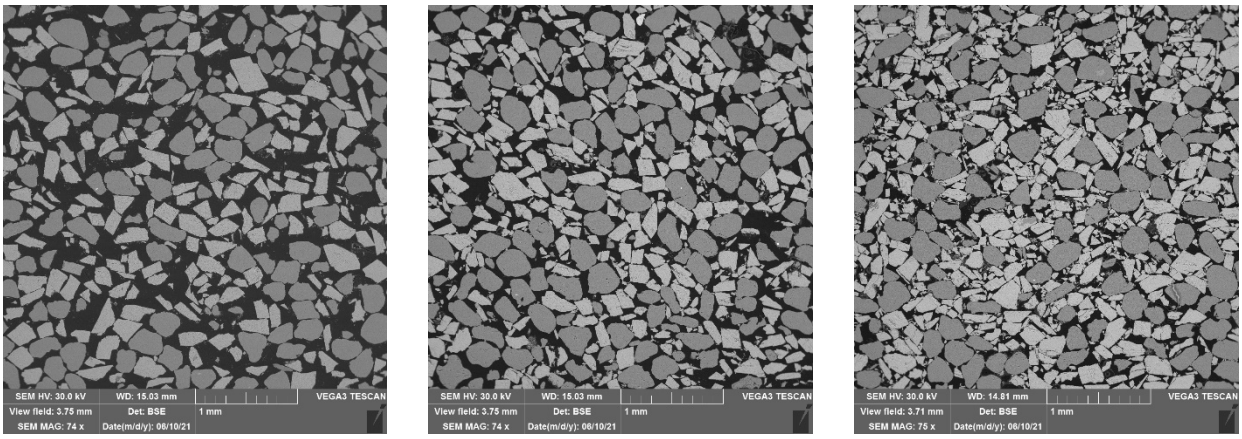

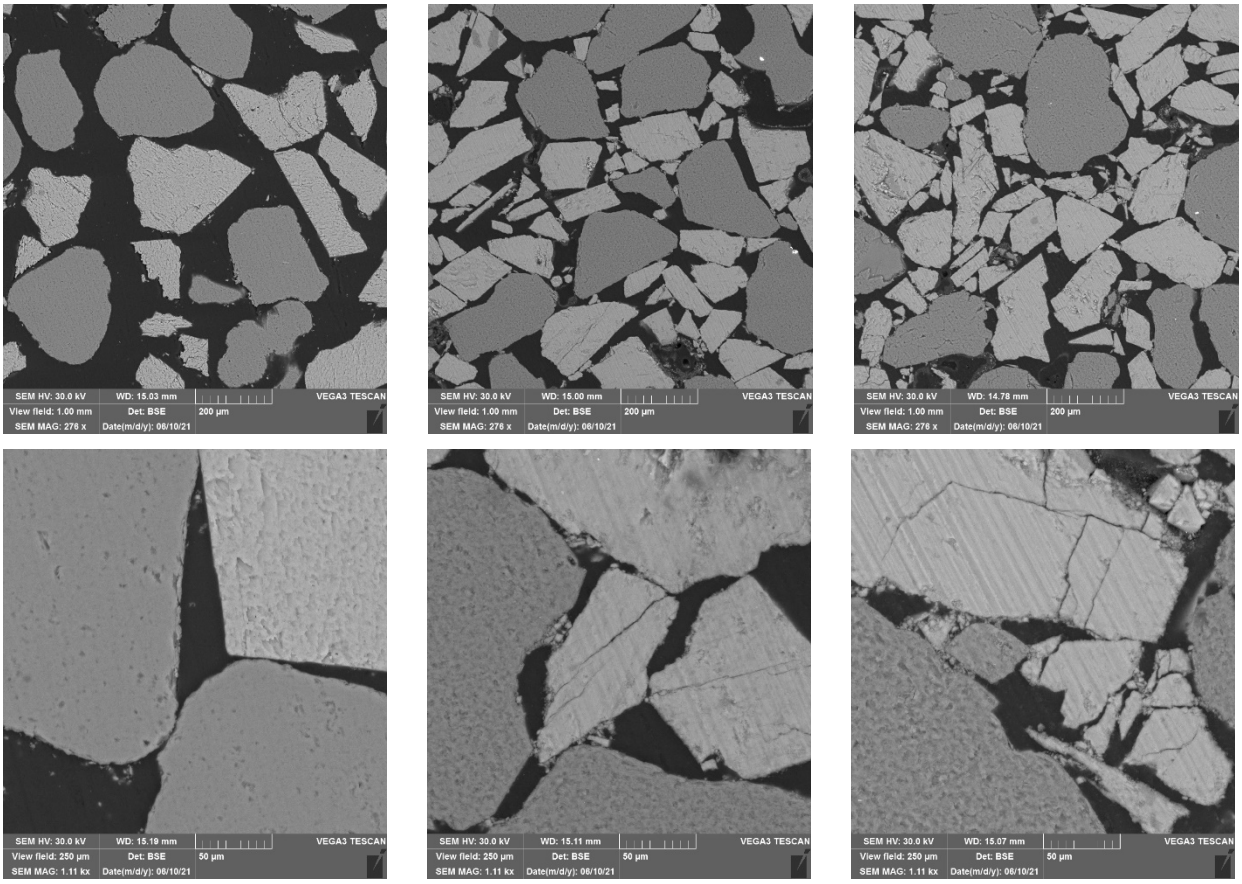


**Figure 4-5. SEM images of starting material (left column), control experiment (middle column), and consolidation experiment (right column). Scale increases with descending rows. Darker grains are quartz, and lighter grains are calcite.**

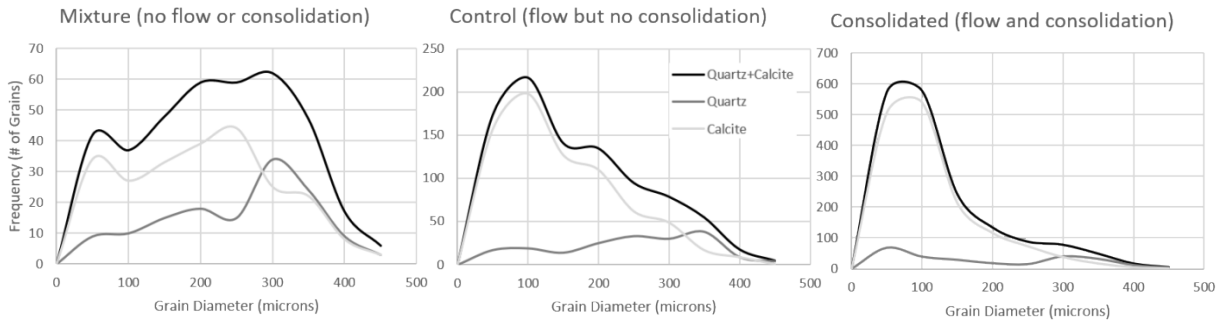


**Figure 4-6. Grain size analysis for starting material (left), control experiment (middle), and consolidation experiment (right).**

As illustrated in the grain-size distribution plots for each sample, calcite grains largely control the overall grain-size distribution for each sample and, during consolidation, may be attributed to occluding some pore spaces that could lead to less fluid flow through the sample (Figures 4-5, 4-6).

High levels of deformation and damage are evident in the consolidation experiment versus the control experiment (**Figures 4-2 – 4-4**). The consolidation experiment reached over 140000 hits at peak stress versus 17 hits for the control experiment (**Figure 4-2**). This level of activity in the consolidation experiment indicates intense levels of damage during pressurization. An increase in rates at around 6 MPa $P_E$ suggests a change in deformation mechanism from grain rearrangement and sliding to widescale fracturing and communition, consistent with our earlier tests on granular calcite (Choens et al., In Review). In the control experiment, AE indicates no sliding or fracture related damage is accruing in this experiment in the absence of loading. Volume loss occurred continuously for the consolidation experiment, while no volume loss occurred under constant pressure conditions for the control experiment (**Figure 4-3**). However, microstructural evidence demonstrated that the control experiment resulted in microfractures, grain size reductions and porosity loss, though it is still substantially less than the consolidation experiment (**Figure 4-6, 4-7**; **Table 4-1**).

**Table 4-1. Fracture and textural analysis of calcite and quartz mixtures for starting material, control experiment, and consolidation experiment.**

| Sample | Average Micro-porosity (%) | Total Micro-fracture Density (mm/mm) | Quartz Micro-fracture Density | Calcite Micro-fracture Density | Modal Grain Diameter (microns) | Calcite Modal Grain Diameter (microns) | Total Grain Perimeter (mm) | Quartz Grain Perimeter (mm) | Calcite Grain Perimeter (mm) |
|---|---|---|---|---|---|---|---|---|---|
| **Starting Material** | -- | 2.2 | 0.4 | 1.8 | 294.6 | 181.5 | 274.8 | 142.4 | 132.4 |
| **Control Exper.** | 30.6 | 5.4 | 1.1 | 4.3 | 64.3 | 34.3 | 455.5 | 173.3 | 282.3 |
| **Conso-lidation Exper.** | 25.1 | 8.9 | 2.1 | 6.8 | 34.7 | 37.8 | 661.3 | 124.2 | 537.1 |

Despite drastic differences in deformation between the consolidation and control experiment, the fluid chemistry results are similar (**Figures 4-3, 4-4**). We attribute this to the abundance of available surface area of calcite and similar extent of calcite dissolution in these two cases. The observed Sr isotope ratios have similar evolutions over time for both experiments (**Figure 4-3**), in agreement with the extent of calcite dissolution being similar in both experiments. Our hypothesis was that the damage induced by consolidation would increase the surface area of calcite and lead to higher calcite dissolution and shifts

in the Sr isotope ratios in the fluid. The collected chemical data in these experiments indicates that too much calcite was available for dissolution reactions in this experiment design. Future work should focus on either grain assemblages with smaller weight percent of calcite (1-10 wt. % in line with carbonate-cemented sandstones), or on actual calcite-containing rock cores, where fracturing will result in new surface area of calcite.

Experimental choices made to achieve the mechanical objective may have hindered chemical objective. The intention was to create a sample with high levels of fracturing in calcite to create an observable signal in fluid chemistry. Hydrostatic consolidation load paths, past the onset of grain crushing, result in high levels of fracturing arising due to stress concentrations at grain contacts. Balancing calcite with stiffer quartz grains both simulated natural clastic reservoirs and preferentially fractured calcite grains in the assemblage (**Figures 4-5**, **4-6**; **Table 4-1**). Rates and temperatures were chosen to prefer fracturing over solution transfer processes. The volume loss during deformation, high levels of AE, and microstructural observations show that the consolidation experiment succeeded from a mechanical perspective. However, samples had high percentages of calcite to generate large numbers of fractures in calcite resulted in significant calcite dissolution, as evidenced by high dissolved Ca levels (as measured by ICP-MS). Fluid samples had to be diluted 100x to bring Ca levels within the detection interval. The abundance of calcite in the sample and extensive calcite dissolution made it difficult to observe changes in surface area due to fracturing. It is also possible that newly created fractures in the consolidation experiment did not see flowing fluids. The consolidation experiment resulted in a large number of intragranular fractures arising at grain contacts, which would be high aspect ratio cracks with low apertures that would be much tighter fluid paths than intergranular pore spaces. Grain rearrangement should reduce intergranular porosity during initial phases of consolidation, but the ease of fluid sampling throughout the experiments suggests high permeability through pore spaces for the duration of the experiment. Fluid sampling was not accessing the newly created fracture faces due to ease of movement through pore spaces and instead measuring the exterior of calcite grains along flow paths. This could also indicate that fluid residence time in between sampling intervals was insufficient but decreasing loading rates to allow for residence times or increasing temperatures could have activated solution transfer processes that are not pertinent to our hypothesis. Fluid sampling intervals during

experiments were also designed to investigate behavior before and after the onset of fracturing; reducing sample intervals could have resulted in incomplete datasets.

### *4.3.3. Conclusions: Consolidation of Calcite-Quartz Assemblages*

Experiments were conducted on granular assemblages of calcite and quartz grains. One experiment was conducted where the sample was consolidated under hydrostatic pressure up to 14.25 MPa $P_E$ with periodic fluid sampling; a second control experiment was conducted with fluid sampling under an effective pressure of 1.25 MPa $P_E$. High volume loss and AE activity indicating deformation and damage can be observed in the consolidation experiment that is not present in the control experiment. Microstructural observations show that fracturing in the consolidation experiment primarily occurs in calcite grains, resulting in a large number of intragranular fractures arising at grain contacts. Control experiments retain the microstructures of the starting material. Despite large differences in deformation and damage, resulting fluid chemistry is similar in magnitude and evolution for both experiments, suggesting the pressure induced fracturing did not alter Sr isotope ratios or calcite dissolution at the scale of these laboratory experiments.

# 5. PUBLICATION IN PREPARATION: MOLECULAR DYNAMICS SIMULATION OF WATER WEAKENING OF CALCITE

To quantify water weakening of calcite, we used a recently developed reactive force field (ReaxFF) parameterized to reproduce the structure, elastic response, and enthalpy of formation of calcite [Dasgupta and Van Duin, unpublished]. ReaxFF is advantageous over the existing classical force fields because it allows for the formation and dissociation of chemical bonds [25]. The current version of the ReaxFF is a significant improvement over an earlier reactive force field for aqueous $CaCO_3$ systems [26]. We used MD simulations to quantify stress-strain behavior of calcite in the absence and presence of water molecules and to identify chemical mechanisms to explain the observed chemo-mechanical trends. Our experimental work (section 4.1), as well as earlier publications [27] indicate that calcite fracturing is promoted by the presence of water. In our MD simulations we observed that the stress-strain curves are sensitive to the size of the domain, the size of initial notch where cracking initiates, as well as whether $CaCO_3$ surface is hydroxylated prior to crack initiation (**Figure 5-1**).

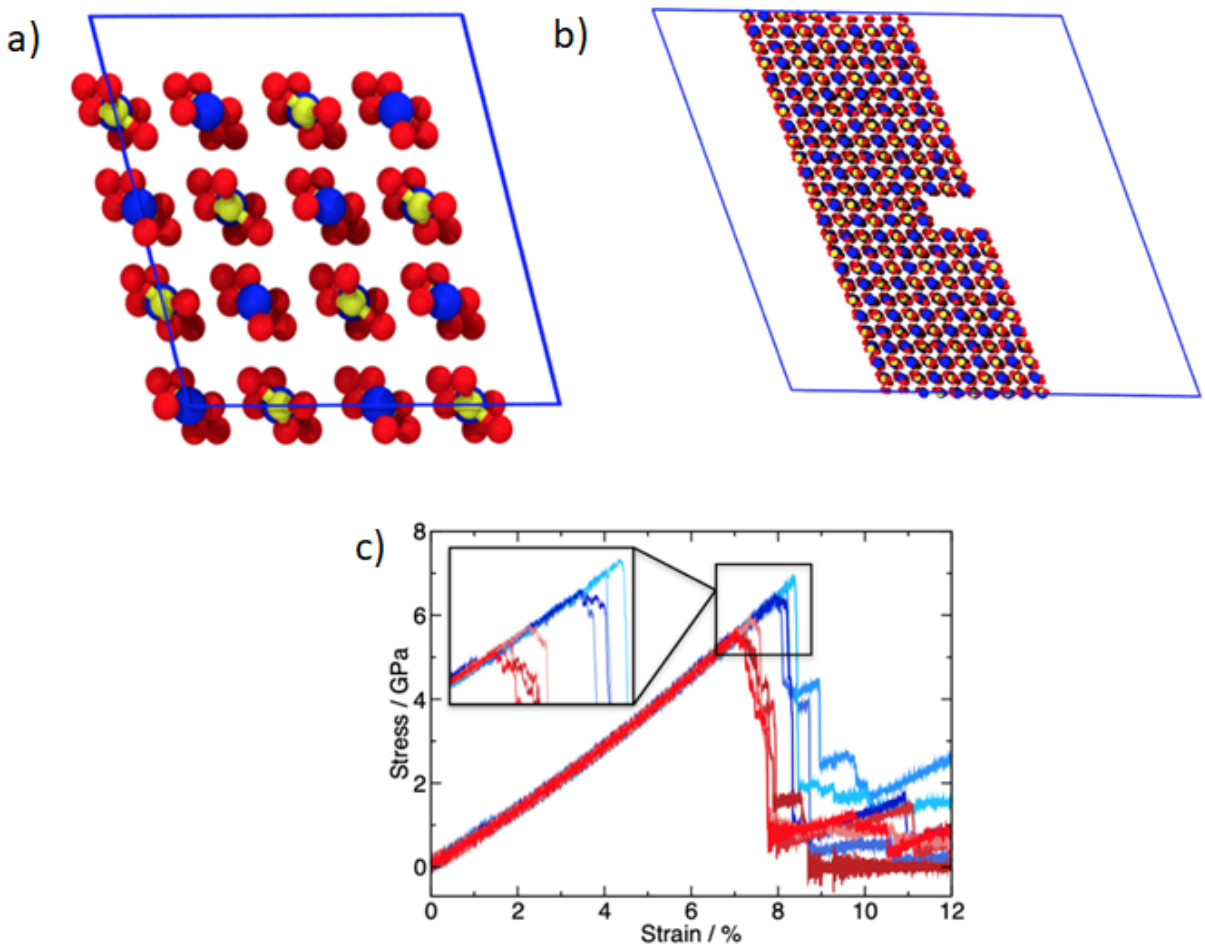


**Figure 5-1. Molecular-scale fracturing of calcite. a) Unit cell of calcite used in molecular dynamics simulations; blue: Ca, yellow: C, red: O; b) Calcite slab with a 2-layer notch, where cracking initiates; c) Stress-strain curves for calcite slabs with different sizes of initial notched region in the absence (red) and presence (blue) of water.**

# 6. PUBLISHED PAPER: CHEMO-MECHANICAL PHASE-FIELD MODELING OF DISSOLUTION-ASSISTED FRACTURE

This paper is published in *Computer Methods in Applied Mechanics and Engineering* journal (https://doi.org/10.1016/j.cma.2020.112838, accepted 7 January 2020) [9].

In this work we showed that chemical dissolution reactions affect the integrity of sedimentary rocks with varying calcite content. We developed a novel phase-field formulation to predict crack propagation in a chemically reactive environment. In this numerical model, chemical damage and mechanical damage are coupled and defined based on the diffusive phase-field fracture method. The chemical damage is also linked to the change in porosity as a result of chemical dissolution and diffusion reactions. We applied this new theoretical framework to three different lithologies, all containing calcite and undergoing exposure to $CO_2$ in geological $CO_2$ storage and enhanced oil recovery scenarios. We demonstrate that this numerical method is able to predict chemo-mechanical coupling and to quantify the impact of chemical alteration on fracturing of realistic rock lithologies (**Figure 6-1**)

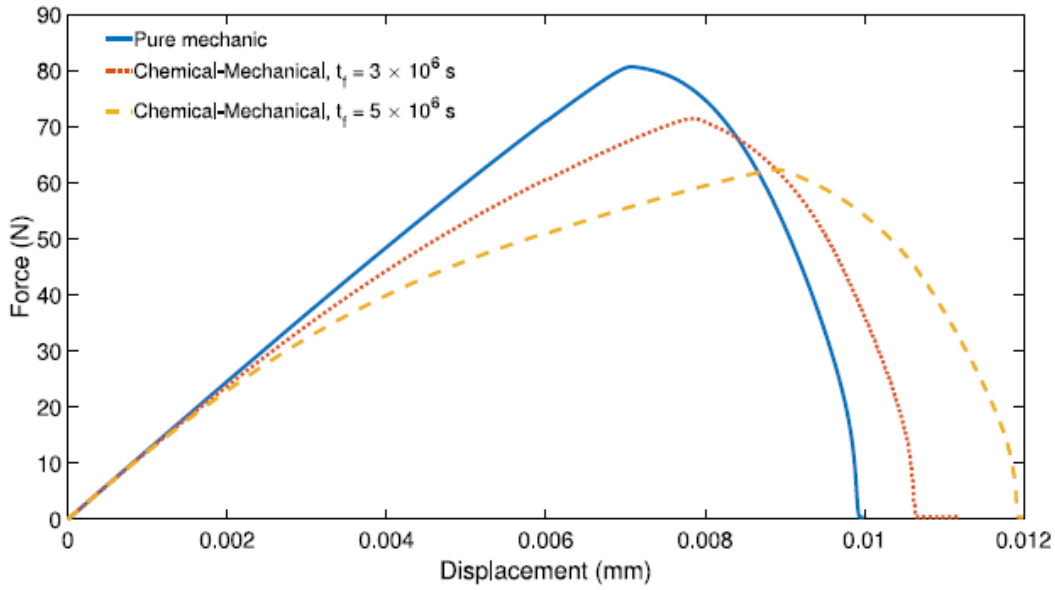


**Figure 6-1. Force-Displacement curves for sandstone lithology with 8 wt.% of calcite. The results indicate with prolonged exposure to $CO_2$, this sandstone becomes weaker (orange curve), compared to unreacted case (blue). Reproduced from L. Schuler, A.G. Ilgen and P. Newell, *Computer Methods in Applied Mechanics and Engineering* 362 (2020) 112838.**

# 7. PUBLICATION IN PREPARATION: THE EFFECT OF LOCAL FLOW FIELDS ON THE DISSOLUTION KINETICS OF $CACO_3$

We developed a numerical framework for simulating calcite dissolution and precipitation measured in microfluidic model fabricated in our laboratory. The geochemical process was described by a system of coupled kinetic and equilibrium reactions, with homogeneous reactions assumed to be in instantaneous equilibrium, and with heterogeneous reactions being kinetically-controlled. This approach is discussed in detail by Lichtner (2018) [28] and commonly used in pore-scale reactive transport modeling (e.g., [29]). The reactive geochemical transport model was implemented in the Sierra/Aria framework [30]. Since mixed equilibrium/kinetic chemical models are not available in Aria, we developed a "plug-in" in this project to solve the equilibrium water reactions locally at each node, given current values of the transported species. The model was validated using an experimental dataset from the literature, and then applied to our experimental results collected using the 3D-printed microfluidic design with a calcite sample (**Figure 7-1**).

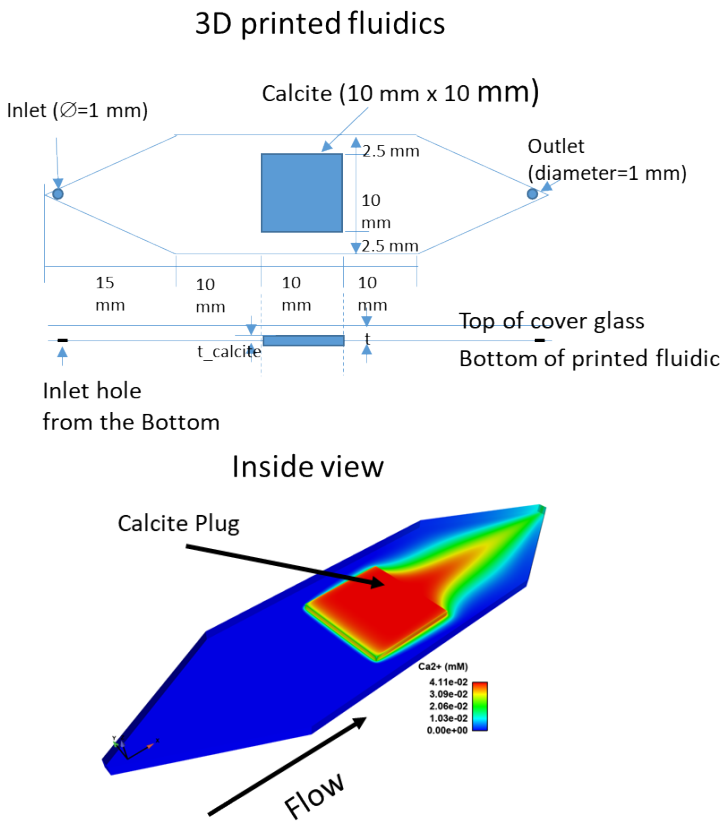


**Figure 7-1. 3D-printed microfluidic design with a square calcite sample in the middle and sample simulation results.**

## REFERENCES


[1] Wiederhold, J.G., *Metal Stable Isotope Signatures as Tracers in Environmental Geochemistry.* Environmental Science & Technology, 2015. **49**(5): p. 2606-2624.

[2] AlKhatib, M. and A. Eisenhauer, *Calcium and strontium isotope fractionation in aqueous solutions as a function of temperature and reaction rate; I. Calcite.* Geochimica Et Cosmochimica Acta, 2017. **209**: p. 296-319.

[3] Tang, J., A. Niedermayr, D.J.Köhler, F. Böhm, B. Kısakürek, A. Eisenhauer, and M. Dietzel, *$Sr^{2+}/Ca^{2+}$ and $^{44}Ca/^{40}Ca$ fractionation during inorganic calcite formation: III. Impact of salinity/ionic strength.* Geochimica et Cosmochimica Acta, 2012. **77**: p. 432-443.

[4] Tang, J.W., S.J. Kohler, and M. Dietzel, *$Sr^{2+}/Ca^{2+}$ and Ca-44/Ca-40 fractionation during inorganic calcite formation: I. Sr incorporation.* Geochimica Et Cosmochimica Acta, 2008. **72**(15): p. 3718-3732.

[5] Fruchter, N., B.Lazar, A. Nishri, A. Almogi-Labin, A. Eisenhauer, Y. Be'eri Shlevin, M. Stein, *Sr-88/Sr-86 fractionation and calcite accumulation rate in the Sea of Galilee.* Geochimica Et Cosmochimica Acta, 2017. **215**: p. 17-32.

[6] Lemarchand, D., G.J. Wasserburg, and D.A. Papanastassiou, *Rate-controlled calcium isotope fractionation in synthetic calcite.* Geochimica et Cosmochimica Acta, 2004. **68**(22): p. 4665-4678.

[7] Jacobson, R.L. and H.E. Usdowski, *Partitioning of strontium between calcite, dolomite and liquids: An experimental study under higher temperature diagenetic conditions, and a model for the prediction of mineral pairs for geothermometry.* Contr. Mineral. and Petrol., 1976. **59**: p. 171-185.

[8] Ilgen, A.G. and R.C. Choens, *Systems and Methods for Controlling Subcritical Fracturing via Chemical Complexation Reactions at the Crack Tip*. Provisional Patent Application SD15492, 2020.

[9] Schuler, L., A.G. Ilgen, and P. Newell, *Chemo-mechanical phase-field modeling of dissolution-assisted fracture.* Computer Methods in Applied Mechanics and Engineering, 2020. **362**, 112838.

[10] Bracco, J.N., M.C. Grantham, and A.G. Stack, *Calcite Growth Rates As a Function of Aqueous Calcium-to-Carbonate Ratio, Saturation Index, and Inhibitor Concentration: Insight into the Mechanism of Reaction and Poisoning by Strontium.* Crystal Growth & Design, 2012. **12**(7): p. 3540-3548.

[11] Bodine, M.W., H.D. Holland, and M. Borcisk. *Co-precipitation of manganese and strontium with calcite*. in *Proc. Symp.,* . 1965. Prague: Problems of Postmagmatic Ore Depostion

[12] Davis, K.J., et al., *Morphological consequences of differential Mg2+incorporation at structurally distinct steps on calcite.* American Mineralogist, 2004. **89**(5-6): p. 714-720.

[13] Declet, A., E. Reyes, and O.M. Suarez, *Calcium carbonate precipitation: A review of the carbonate crystalization process and applications in bio inspired composites. .* Review of Advanced Material Science 2016. **44**: p. 87-107.

[14] Forbes, T.Z., A.V. Radha, and A. Navrotsky, *The energetics of nanophase calcite.* Geochimica Et Cosmochimica Acta, 2011. **75**(24): p. 7893-7905.

[15] Gabitov, R.I., A. Sadekov, and A. Leinweber, *Crystal growth rate effect on Mg/Ca and Sr/Ca partitioning between calcite and fluid: An in situ approach.* Chemical Geology, 2014. **367**: p. 70-82.

[16] Gabitov, R.I. and E.B. Watson, *Partitioning of strontium between calcite and fluid.* Geochemistry Geophysics Geosystems, 2006. **7**.

[17] Hodkin, D.J., D.I. Stewart, J.T. Graham, G. Cibin, and I.T. Burke., *Enhanced Crystallographic Incorporation of Strontium(II) Ions into Calcite via Preferential Adsorption at Obtuse Growth Steps.* Crystal Growth & Design, 2018. **18**(5): p. 2836-2843.

[18] Ichikuni, M., *Partition of Strontium between Calcite and Solution - Effect of Substitution by Manganese.* Chemical Geology, 1973. **11**(4): p. 315-319.

[19] Katz, A., E. Sass, A. Starinsky, H.D. Holland, *Strontium Behavior in Aragonite-Calcite Transformation - Experimental Study at 40-98 Degrees C.* Geochimica Et Cosmochimica Acta, 1972. **36**(4): p. 481.

[20] Mucci, A. and J.W. Morse, *The Incorporation of $Mg^{2+}$ and $Sr^{2+}$ into Calcite Overgrowths - Influences of Growth-Rate and Solution Composition.* Geochimica Et Cosmochimica Acta, 1983. **47**(2): p. 217-233.

[21] Nielsen, M.R., K.K. Sand, J.D. Rodriguez-Blanco, N. Bovet, J. Generosi, K.N. Dalby, and S.L.S. Stipp, *Inhibition of Calcite Growth: Combined Effects of $Mg^{2+}$ and $SO_4^{2-}$.* Crystal Growth & Design, 2016. **16**(11): p. 6199-6207.

[22] Olszta, M.J., S. Gajjeraman, M. Kaufman, and L.B. Gower, *Nanofibrous Calcite Synthesized via a Solution−Precursor−Solid Mechanism.* Chemistry of Materials, 2004. **16**(12): p. 2355-2362.

[23] Pingitore, N.E. and M.P. Eastman, *The coprecipitation of $Sr^{2+}$ with calcite at 25° C and 1 atm.* Geochimica et Cosmochimica Acta, 1986. **50**(10): p. 2195-2203.

[24] Tesoriero, A.J. and J.F. Pankow, *Solid solution partitioning of $Sr^{2+}$, $Ba^{2+}$, and $Cd^{2+}$ to calcite.* Geochimica Et Cosmochimica Acta, 1996. **60**(6): p. 1053-1063.

[25] Van Duin, A.C., et al., *ReaxFF: a reactive force field for hydrocarbons.* The Journal of Physical Chemistry A, 2001. **105**(41): p. 9396-9409.

[26] Gale, J.D., P. Raiteri, and A.C. Van Duin, *A reactive force field for aqueous-calcium carbonate systems.* Physical Chemistry Chemical Physics, 2011. **13**(37): p. 16666-16679.

[27] Ilgen, A.G., et al., *Chemical controls on the propagation rate of fracture in calcite.* 2018. **8**(1): p. 16465.

[28] Lichtner, P.C., *Continuum formulation of multicomponent-multiphase reactive transport*, in *Reactive transport in porous media*. 2018, De Gruyter. p. 1-82.

[29] Yoon, H., Q. Kang, and A.J. Valocchi, *Lattice Boltzmann-based approaches for pore-scale reactive transport.* Reviews in Mineralogy and Geochemistry, 2015. **80**(1): p. 393-431.

[30] *SIERRA multimechanics module: Aria user manual–version 4.56.* Sandia Report No. SAND2020-4000, Sandia National Laboratories, 2020.

# DISTRIBUTION

**Email—Internal**

| Name | Org. | Sandia Email Address |
|---|---|---|
| R. Charles Choens | 08914 | rcchoen@sandia.gov |
| Haley J. Davis | 08915 | hjdavis@sandia.gov |
| Jacob A. Harvey | 08915 | jharve@sandia.gov |
| Anastasia G. Ilgen | 08915 | agilgen@sandia.gov |
| Andrew W. Knight | 08845 | aknigh@sandia.gov |
| Mario J. Martinez | 01516 | mjmarti@sandia.gov |
| Melissa M. Mills | 08844 | mmmills@sandia.gov |
| Jennifer Wilson | 08914 | jenwils@sandia.gov |
| Hongkyu Yoon | 08914 | hyoon@sandia.gov |
| Technical Library | 01977 | sanddocs@sandia.gov |

This page left blank

Sandia National Laboratories

Sandia National Laboratories is a multimission laboratory managed and operated by National Technology & Engineering Solutions of Sandia LLC, a wholly owned subsidiary of Honeywell International Inc. for the U.S. Department of Energy's National Nuclear Security Administration under contract DE-NA0003525.